Approaching the thermodynamic limit of a bounded one-component plasma

D. I. Zhukhovitskii^{1,*} and E. E. Perevoshchikov^{2,1}

¹ Joint Institute of High Temperatures, Russian Academy of Sciences, Izhorskaya 13, Bd. 2, Moscow, 125412 Russia ² Moscow Institute of Physics and Technology, Institutskiy Pereulok 9, Dolgoprudny, Moscow Region, 141701 Russia (Dated: November 7, 2025)

The classical one-component plasma (OCP) bounded by a spherical surface reflecting ions (BOCP) is studied using molecular dynamics (MD). Simulations performed for a series of sufficiently large BOCP's make it possible to establish the size dependencies for the investigated quantities and extrapolate them to the thermodynamic limit. In particular, the total electrostatic energy per ion is estimated in the limit of infinite BOCP in a wide range of the Coulomb coupling parameter Γ from 0.03 to 1000 with the relative error of the order 0.1%. Calculated energies are by about 0.5% lower as compared to the modern Monte Carlo (MC) simulation data obtained by different authors at $\Gamma < 30$ and almost coincide with the MC results at $\Gamma > 175$. We introduce two more converging characteristic energies, the excess interatomic electrostatic energy and the excess ion–background electrostatic energy, which enable us to calculate the ionic compressibility factor inaccessible in conventional MC and MD simulation of the OCP with periodic boundary conditions. The derived wide-range ionic equation of state can be recommended for testing OCP simulations with various effective interaction potentials. Based on this equation, we propose an improved cutoff radius for the interionic forces implemented in LAMMPS and perform MD simulation of the OCP to demonstrate that location of the metastable region of the fluid–solid phase transition depends sensitively on this radius

PACS numbers: 52.27.Gr,52.25.Kn,52.65.-y,36.40.Ei

I. INTRODUCTION

A system of equal pointlike charges immersed in a uniform neutralizing background of fixed charge density is known as the one-component plasma (OCP) [1–4]. This model is widely explored due to its simplicity that allows one to develop and test models for weakly and, especially, for strongly coupled plasmas. Introduction of a rigid background (although, some OCP modifications allow for the compressible background) is a convenient way to avoid instability of the Coulomb systems. In addition to an obvious importance of the OCP model for the theory, it has no less important applications in astrophysics because it is appropriate for the interiors of white dwarfs [5–10], neutron stars [11], and for liquid alkali metals [12]. OCP turns out to be effective for such localized nonneutral plasma objects as trapped ions [13, 14] and the Coulomb clusters (Coulomb balls) in dusty plasmas [15– 19] as well as for quasi-homogeneous dust plasma [20, 21]. Besides the classical OCP, quantum OCP is widely studied [22, 23], many more of them, in application to astrophysics [24–26]. The screened Coulomb (or Yukawa) systems are being studied no less intensively [27–32]. In some studies, properties of the classical OCP are deduced in a limiting case of the Yukawa system with the infinite Debye length.

For the classical OCP, most studied are the internal and Helmholtz free energy and the equation of state. Investigations are performed using analytical methods [32–39], Monte Carlo (MC) [40–47] and molecular dynamics

(MD) simulation [48]. Extrapolation of the MC data to infinite number of ions makes it possible to obtain the most accurate (with the relative error about 0.1% and better) estimation of the system electrostatic energy. Extensively studied is melting of the OCP [49–53], the liquidlike to gaslike dynamical crossover [21, 54, 55]; the OCP transport properties are also of interest [55].

Conventional conditions used in OCP simulations are periodic boundary conditions (PBC) that are inevitable in the case of long-range Coulomb forces. Since for such a system, electrostatic energy is represented as a series with conditional convergence, a method based on summation in reciprocal space developed by Ewald [56] (see also [57]) is used along with the modifications increasing its efficiency (e.g., [58–60]). For the PBC (or bulk) OCP, a single converging energy characteristic is the system total electrostatic energy per ion, at least, no other converging quantity can be obtained directly from the Ewald summation. In contrast, finite-size systems with the finite number of ions N and an explicit boundary offer a possibility to search for such characteristics because each of them becomes formally finite and can be calculated directly by summation of individual Coulomb interactions, which does not require the Ewald summation. As is known [61], every Coulomb system reaches a thermodynamic limit at $N \to \infty$. Therefore, if it is possible to establish a size dependence for the quantity of interest or to demonstrate that it is almost size-independent at sufficiently large N then a reliable extrapolation to the thermodynamic limit can be derived.

In our recent study [62], we investigated large Coulomb clusters with a spherical neutralizing background at $\Gamma \gtrsim 200$ and demonstrated that for N > 2500, a quasi-homogeneous cluster core can be found that can be

^{*} dmr@ihed.ras.ru

treated as a satisfactory approach to the bulk system with compatible characteristics. We showed that the ionic compressibility factor Z_i could be expressed in terms of the energies of interionic interaction and their interaction with the cluster background. However, we succeeded in a very crude estimation of Z_i only at $\Gamma=500$ because the ion evaporation breaks noticeably both the system stability and its local quasineutrality at lower Γ .

In this work, we consider the model of bounded OCP (BOCP) that is free from these shortcomings, in which a rigid boundary reflecting the ions specularly is situated at the surface of the background sphere. In this model, it is possible to investigate the entire range of Γ from weakly to strongly coupled systems and to determine the size dependence for the quantities of interest. In addition to the conventional total electrostatic energy, we introduce two more energy quantities, the excess interatomic and ion-background electrostatic energy, and show them to be convergent in the thermodynamic limit. We also deduce the ionic pressure, i.e., the pressure of the ionic subsystem, as a linear combination of these energies. This enabled us to construct the ionic equation of state verified by determination of the ionic virial, which must hold for ordinary OCP.

Yet another problem associated with the reciprocal space summation is an explicit dependence of the resulting interionic effective potential on the simulation cell length, which proves to be the potential decay length. This means that the Ewald potential, although decaying much more rapidly than the Coulomb one, is still the slowly decaying one. This is a source of ambiguity in taking into account the interaction of ions with their periodic images, which was noted already in the early study [40]. The most sensitive to this ambiguity is MD simulation, so that alternative methods for summation in the k-space were proposed like [58], in which the contribution from neighboring ions at the distance less than r_c are included directly while that of distant ions are calculated by the k-space summation. Onegin et al. [63] first discovered that the virial determined in the MD simulation of OCP depends strongly on r_c , and moreover, this virial disagrees strongly with the pressure that is derived from the system potential energy. Again, the ab initio BOCP simulation does not encounter such problem, and we can compare the ionic pressure from our simulation with that for OCP. Thus, we propose to "fix" the MD simulations for OCP by taking r_c as a function of Γ when our Z_i is used as reference data. As an illustration, we demonstrate that a different choice of r_c changes drastically the width of metastable region of fluid-solid phase transition thus indicating the change in interfacial surface tension.

In Sec. II A, we introduce the main BOCP energy characteristics and explore them in limiting cases; in Sec. II B, we derive the ionic equation of state as well as its excess ionic Helmholtz free energy. The method of MD simulation along with its justification and typical parameters is presented in Sec. III A. In Sec. III B, the MD results for BOCP are analyzed and discussed. Secs. IV A and

IV B are devoted to the MD simulation of the OCP with PBC: the details of simulation method are discussed in Sec. IV A; in Sec. IV B, the recommended dependence $r_c(\Gamma)$ is presented, and the effect of this dependence on the kinetics of fluid–solid transition is illustrated.

II. THEORETICAL BACKGROUND

A. Energy characteristics of the bounded one-component plasma

We treat a system of N particles (ions) with the mass m and charge ze, where e is the elementary charge, on a uniform background of the total charge -zeN bounded by a sphere of the radius R. To prevent ion evaporation at high temperature, i.e., departure of the faster ions to infinity, the system is bounded by a rigid spherical boundary, from which the ions are reflected specularly. Since we develop an asymptotic model of the OCP, its radius R_b must coincide with that of the background; otherwise, the system cannot be homogeneous even at low Γ . However, finiteness of the MD integration time step requires that R_b is somewhat less than R (Sec. III A).

In what follows, we will term such system the BOCP. In contrast to OCP, here, another key parameter N is added to the Coulomb coupling parameter $\Gamma = \epsilon/T$, where $\epsilon = z^2 e^2/r_s$ is the characteristic energy, $r_s = (3/4\pi\bar{n})^{1/3} = RN^{-1/3}$ is the ion sphere radius, $\bar{n} = 3N/4\pi R^3$ is the average ion number density, T is the temperature in energy units; BOCP is assumed to be in the equilibrium state, and N is sufficiently large. Hereafter, we will use the Coulomb units such as the length r_s , the energy ϵ , and the time $\tau_0 = r_s(m/\epsilon)^{1/2} = (mr_s^2/\Gamma T)^{1/2}$, which coincides with the inverse oscillation frequency of an ion in the ion sphere (in these units, $T = 1/\Gamma$, $R = N^{1/3}$, and $\bar{n} = 3/4\pi$).

The total electrostatic energy of the BOCP per ion is

$$u(\Gamma, N) = u_p + u_b + u_c, \tag{1}$$

where

$$u_p = \frac{1}{N} \sum_{k < l} \frac{1}{r_{kl}} = \frac{1}{2N} \iint_{V_R} \frac{n(\mathbf{r}'_1)n(\mathbf{r}'_2)}{r'_{12}} d\mathbf{r}'_1 d\mathbf{r}'_2$$
 (2)

is the interionic interaction energy per ion, $r_{12} = |\mathbf{r}_1 - \mathbf{r}_2|$, $n(\mathbf{r}') = \sum_{k=1}^{N} \delta(\mathbf{r}' - \mathbf{r}_k)$ is the ion number density, \mathbf{r}_k is the radius-vector of the kth ion, and the integration is performed in the background volume V_B ;

$$u_b = \frac{1}{2N} \sum_{k=1}^{N} r_k^2 - \frac{5}{2} u_c$$

$$= \frac{1}{2N} \int_{V_R} {r'}^2 n(\mathbf{r}') d\mathbf{r}' - \frac{5}{2} u_c$$
(3)

is the energy of interaction between the ions and background per ion, and

$$u_c = \frac{3}{5}N^{2/3} \tag{4}$$

is the background energy per ion. Equation (3) implies that origin of the coordinate system coincides with the background center. Although u converges at $N \to \infty$, u_p and u_b diverge as $N^{2/3}$; however, one can define renormalized quantities that will be termed the excess interatomic and ion–background electrostatic energy

$$u_{pex} = u_p - u_c, \quad u_{bex} = u_b + 2u_c, \tag{5}$$

respectively, such that the total energy $u = u_{pex} + u_{bex}$ coincides with the excess total electrostatic energy.

We will demonstrate convergence of u_{pex} and u_{bex} in the cases of weakly and strongly coupled systems. If the system is gaslike, and the ternary and higher ion correlations can be neglected, then

$$\langle n(\mathbf{r}_1)n(\mathbf{r}_2)\rangle = \langle n(0)n(r_{12})\rangle = \left(\frac{3}{4\pi}\right)^2 f_p(r_{12}),$$
 (6)

where angular brackets denote time averaging, and

$$f_p(r) = \frac{1}{3r^2} \frac{dN_r}{dr} \tag{7}$$

is the radial distribution function and N_r is the average number of ions within a sphere of the radius r around an ion. Similarly, $\langle n(\mathbf{r}) \rangle = \langle n(r) \rangle = (3/4\pi)f_c(r)$, where

$$f_c(r) = \frac{1}{3r^2} \frac{dN_c}{dr} \tag{8}$$

is the ion density distribution and N_c is the average number of ions at the distance not larger than r from the background center. Then from Eqs. (2) and (3) we obtain

$$\langle u_{pex} \rangle \simeq \frac{1}{2N} \left(\frac{3}{4\pi} \right)^2 \iint_{V_R} \frac{f_p(r_1) f_p(r_2) - 1}{r_{12}} d\mathbf{r}_1 d\mathbf{r}_2$$

$$= \frac{9}{4N} \int_0^R \int_0^R [f_p(r_1) f_p(r_2) - 1]$$

$$\times (r_1 + r_2 - |r_1 - r_2|) r_1 r_2 dr_1 dr_2$$
(9)

and

$$\langle u_{bex} \rangle \simeq \frac{3}{2N} \int_{0}^{R} r^4 \left[f_c(r) - 1 \right] dr.$$
 (10)

Since the ion correlations decay at $\Gamma \to 0$, then $f_p, f_c \to 1$, and from Eqs. (9) and (10), it follows that

$$\lim_{\Gamma \to 0} \langle u_{pex} \rangle = \lim_{\Gamma \to 0} \langle u_{bex} \rangle = 0.$$
 (11)

Thus, in the thermodynamic limit, we obtain an obvious result: all excess electrostatic energies of ideal gas vanish:

$$\lim_{N \to \infty} \lim_{\Gamma \to 0} \langle u_{\text{pex}} \rangle = \lim_{N \to \infty} \lim_{\Gamma \to 0} \langle u_{\text{bex}} \rangle = u_{\infty} = 0, \quad (12)$$

where $u_{\infty} = \lim_{N \to \infty} \langle u \rangle$. Note that if we treat separately the system of ions in the field of background then the system potential energy $u_i = u_p + u_b$ diverges as $N \to \infty$. However, the excess potential energy $u_i + u_c = u_{pex} + u_{bex}$ does converge.

Consider the case $\Gamma \to \infty$, in which the ion sphere model (see, e.g., [2]) proved to be most effective for the Coulomb clusters [62, 64]. This model implies that the entire system is divided into spherical overlapping spheres of the radius r_s , in which single ions reside, and all interparticle and particle–background interaction can be reduced to the interaction of an ion with the compensating background of its sphere. Thus, the net force acting on an ion is simply $\mathbf{f} = -\mathbf{r}$, where the origin of the coordinate system is shifted to the center of an ion sphere and we omit subscripts due to identity of the ions. Based on the virial theorem [65] and an obvious equality for a harmonic oscillator $\langle r^2 \rangle = \langle v^2 \rangle = 3/\Gamma$, we can write the ion compressibility factor as [62]

$$Z_i = 1 + \frac{\Gamma}{3N} \sum_{i=1}^{N} \langle \mathbf{rf} \rangle = 1 - \frac{\Gamma}{3} \langle r^2 \rangle = 0,$$
 (13)

i.e., the ionic compressibility factor along with the ionic pressure p_i vanish at $\Gamma \to \infty$.

We will use the virial theorem one more time to express the ion pressure and corresponding compressibility factor in terms of the ion subsystem potential and kinetic energy. However, if we assume that the charge neutralizing background of BOCP is fixed, $r_s = \text{const}$, then the energy $u_p(2)$ is a homogeneous function of order -1, $u_b + 5u_c/2$, of order 2 (Eq. (3)), and u_c , of order 0. Bearing in mind that if the function φ is a sum of homogeneous functions of order k, $\varphi(x) = \sum_k \psi_k(x)$, then

$$\frac{d\varphi}{dx} = \sum_{k} \frac{k\psi_k(x)}{x},\tag{14}$$

and one can modify the virial theorem for the ions in the field of background as

$$3p_i V_R = \frac{3}{\Gamma} + u_p - 2u_b - 5u_c, \tag{15}$$

where $3/\Gamma$ is the kinetic energy of an ion, whence it follows that [62]

$$Z_i = \frac{p_i V_R}{NT} = 1 + \frac{\Gamma}{3} (u_{pex} - 2u_{bex}).$$
 (16)

Here and in what follows, the energy quantities will be implied time averaged, and corresponding notation will be omitted.

From Eqs. (13) and (16),

$$\lim_{\Gamma \to \infty} \frac{Z_i - 1}{\Gamma} = \lim_{\Gamma \to \infty} (u_{pex} - 2u_{bex}) = 0.$$
 (17)

At the same time, $\lim_{N\to\infty}\lim_{\Gamma\to\infty}u=\lim_{N\to\infty}\lim_{\Gamma\to\infty}(u_{pex}+u_{bex})=u_0$, where $u_0=-0.8959293$ is the Madelung constant for the bcc lattice. Hence,

$$\lim_{N \to \infty} \lim_{\Gamma \to \infty} u_{pex} = \frac{2}{3} u_0, \quad \lim_{N \to \infty} \lim_{\Gamma \to \infty} u_{bex} = \frac{1}{3} u_0. \quad (18)$$

Obviously, (18) hold in the thermodynamic limit $N \to \infty$. Thus, we have demonstrated that the quantities (5) have thermodynamic limits at low and high Γ , which is indicative of the fact that these limits exist at arbitrary Γ defining the ionic pressure for the bulk OCP.

Since an objective of this paper is investigation of the OCP properties, the size dependence $u(\Gamma, N)$ (1) is of interest. As it was demonstrated in [62], all quantities derived from the BOCP energy characteristics depend on N very weakly, therefore, we adopt $\ln N$ as an argument. The simplest and most general form of the size dependence is then the expansion in powers of shifted $\ln N$, where we retain solely two terms:

$$u(\Gamma, N) = u_{\infty}(\Gamma) + \frac{c_1(\Gamma)}{\ln N + c_2(\Gamma)}.$$
 (19)

Here, c_1 and c_2 are the parameters to be defined from fitting the MD simulation results (Sec. III B).

B. Equations of state and thermodynamic functions

In Sec. II A, we have explored the ionic subsystem and derived the equation of state (EOS) (16) for it. Below, we will obtain EOS for the entire system, which is supposed to include a contribution from the background. Hence, this requires some physical idea of the background nature. We consider the simplest model of the background as a system of a large number $\bar{N} \to \infty$ of small charged pseudo-particles of the charge $\bar{z}e$ uniformly distributed in the volume V_R such that $N\bar{z} + Nz = 0$ [50]. Here, the quantities related to the pseudo-particles are marked by bar. In this limit, it is obvious that both the pseudo-particle-pseudo-particle and pseudo-particleion coupling parameters, $\Gamma(N/\bar{N})^{5/3}$ and $\Gamma(N/\bar{N})^{2/3}$, respectively, vanish, and the background electrostatic energy is defined by Eq. (4). Now, we have to treat the system potential energy as a homogeneous function of the coordinates of the order -1 and write the equation of state for the entire system based on the virial theorem as

$$p = \frac{N}{V_R} \left(T + \frac{2K}{3N} - \frac{u}{3} \right), \tag{20}$$

where p is the system pressure and $\bar{K} = (3/2)\bar{N}T$ is the pseudo-particle kinetic energy. As is well-known, the totally neutral system of classical Coulomb charges tends

to collapse, and the main background function is to stabilize the entire system. This is reached by the ideal gas pressure of the pseudo-particles, which tends to infinity as $\bar{N} \to \infty$. However, one can renormalize this pressure by introducing the excess pressure $p \to p - 2\bar{K}/3V_R$ [50], so that the compressibility factor is reduced to

$$Z = 1 + \frac{\Gamma u}{3} \tag{21}$$

(see, cf. [40]). In terms of virials, Eq. (20) with $\bar{K}=0$ can be written as

$$p = \frac{N}{V_R} \left(T + \frac{1}{3N} \sum_{i=1}^{N} \langle \mathbf{r}_i \mathbf{f}_i \rangle + \frac{1}{3N} \sum_{j=1}^{\bar{N}} \langle \bar{\mathbf{r}}_j \bar{\mathbf{f}}_j \rangle \right), \quad (22)$$

whereas the expression for p_i (15) corresponds to

$$p_i = \frac{N}{V_R} \left(T + \frac{1}{3N} \sum_{i=1}^{N} \langle \mathbf{r}_i \mathbf{f}_i \rangle \right)$$
 (23)

and (16), to

$$Z_i = 1 + \frac{\Gamma}{3N} \sum_{i=1}^{N} \langle \mathbf{r}_i \mathbf{f}_i \rangle. \tag{24}$$

The pressures p and p_i and corresponding compressibility factors Z and Z_i differ by the third term in parenthesis on the right-hand side of (22), which cannot be determined in any simulation. Therefore, although the pressure (22) must be fully compatible with its thermodynamic definition because it leads to (21), it is impossible to obtain it from simulations. Incompatibility of the pressure defined thermodynamically with that obtained from the virial was noted in study [63], where a different interpretation for such discrepancy was formulated. Note that the ionic pressure (15) and (23) are compatible with thermodynamics and can be determined directly from MD simulation. In addition, it is the only pressure that positively has physical meaning.

If we treat the ions in the field of background as a separate system, we can define the excess internal energy of the ions $\varepsilon_{iex}(\Gamma, N)$ per ion. Since at T = 0, $u_i = u_p + u_b = u_0 - u_c$, relative to this reference state,

$$\varepsilon_{iex}(\Gamma, N) = u(\Gamma, N) - u_0$$
 (25)

depends on the total system electrostatic energy. Note that $\varepsilon_{iex}(\Gamma, N)$ has a thermodynamic limit, while $u_p + u_b$ does not. In the thermodynamic limit, at $\Gamma > \Gamma_m$, where $\Gamma = \Gamma_m$ is the melting point of OCP, the harmonic lattice model is applicable [26, 66], in which

$$\varepsilon_{iex}(\Gamma, \infty) = \frac{3}{2\Gamma} + \frac{\beta_2}{\Gamma^2},$$
 (26)

with the coefficient β_2 defining anharmonicity. The thermodynamic limit of the excess ionic Helmholtz free energy per ion that can be calculated from (25) using (see,

e.g. [35]),

$$f_{iex}(\Gamma) = -\int_{\Gamma}^{\infty} \frac{\varepsilon_{iex}(\Gamma', \infty)}{\Gamma'} d\Gamma',$$
 (27)

is a function of $u_{\infty}(\Gamma)$. If $\Gamma_{\rm m}$ and β_2 are known, the excess ionic Helmholtz free energy, which coincides with this quantity for the entire system, can be derived using (26):

$$f_{i\rm ex}(\Gamma_{\rm m}) = -\frac{3}{2\Gamma_{\rm m}} - \frac{\beta_2}{2\Gamma_{\rm m}^2}.$$
 (28)

III. MD SIMULATION FOR BOCP

A. Simulation method

An advantage of the BOCP simulation is absence of diverging quantities due to finiteness of N, which makes it possible to determine all quantities of interest including u, u_p , and u_b . In contrast, calculation of the total potential energy u for the OCP with PBC requires application of special summation methods such as the Ewald potential [40, 56], angular-averaged Ewald potential [47], particle-particle particle-mesh method (PPPM) [67], etc., while for BOCP, this quantity can be determined ab initio from direct summation of the interparticle Coulomb energies and the particle-background energy. Moreover, since no summation method for u_{pex} and u_{pex} for OCP has been developed, BOCP simulation remains a unique method for estimation of these quantities. Obvious shortcomings of the BOCP simulation are enormous computational efforts when no acceleration procedure is possible and the necessity to simulate a whole spectrum of the BOCP sizes to enable the extrapolation to the thermodynamic limit.

MD simulation of ions motion within the background sphere is performed. Introduction of the dimensionless dynamic quantities by replacement for the time $t \to t/\tau_0$, the radius-vector of the *i*th ion $\mathbf{r}_i \to \mathbf{r}_i/r_s$, and the force acting on this ion $\mathbf{f}_i \to (r_s/\varepsilon)\mathbf{f}_i = (\tau_0^2/mr_s)\mathbf{f}_i$ makes it possible to write the equation of the ion motion in the form [62]

$$\ddot{\mathbf{r}}_i = \mathbf{f}_{zi} + \mathbf{f}_{bi} + \mathbf{f}_{Li},\tag{29}$$

where

$$\mathbf{f}_{zi} = \sum_{j \neq i} \frac{\mathbf{r}_i - \mathbf{r}_j}{r_{ij}^3} \tag{30}$$

is the force of interparticle interaction,

$$\mathbf{f}_{bi} = -\mathbf{r}_i \tag{31}$$

is the force of attraction to the background, and

$$\mathbf{f}_{Li} = -\gamma \dot{\mathbf{r}}_i + \mathbf{f}_{\text{st}i} \tag{32}$$

is the force acting from the Langevin thermostat. Here, γ is the particle friction coefficient, $\mathbf{f}_{\mathrm{s}ti}$ is a random force with the Gaussian distribution such that

$$\langle f_{\rm sti}^2 \rangle = \frac{2\gamma \langle v^2 \rangle}{\tau_{\rm st}} = \frac{6\gamma}{\Gamma \tau_{\rm st}},$$
 (33)

where $\tau_{\rm st}$ is the autocorrelations decay time, which was set equal to the time integration step τ , $\langle v^2 \rangle \equiv \langle v_i^2 \rangle$ is the mean squared ion velocity, which is independent of i at equilibrium, and we take into account that in equilibrium, $\langle v^2 \rangle = 3T = 3/\Gamma$.

A contact with the thermostat in the course of simulation reduces sharply the system equilibration time and ensures a very small deviation of $\langle v^2 \rangle/3$ from the desired value T thus decreasing sharply the computation time. However, the question arises whether the inclusion of f_{Li} in the total force can distort the virial. Below, we demonstrate that no distortion can be observed because $\sum_{i=1}^{N} \mathbf{r}_i \mathbf{f}_{Li} = 0$. First, consider the case of ideal gas $(\Gamma \to 0)$, then Eq. (29) can be rewritten as

$$\ddot{\mathbf{r}}_i = -\gamma \dot{\mathbf{r}}_i + \mathbf{f}_{\text{st}i}.\tag{34}$$

We take the dot products of both sides of (34) and \mathbf{r}_i , average this equation, and take into account that $\langle \mathbf{r}_i \ddot{\mathbf{r}}_i \rangle = d \langle \mathbf{r}_i \dot{\mathbf{r}}_i \rangle / dt - \langle v^2 \rangle$ and

$$\frac{d}{dt} \langle \mathbf{r}_i \dot{\mathbf{r}}_i \rangle = \frac{1}{2} \frac{d^2}{dt^2} \langle r_i^2 \rangle = \frac{D}{2} \frac{d^2 t}{dt^2} = 0, \tag{35}$$

where we imply that an ion is involved in the Brownian motion when $\langle r_i^2 \rangle = Dt$ with the diffusion coefficient $D = \tau_{\rm st} \langle v^2 \rangle$. Bearing this in mind we infer from Eqs. (33) and (34) that $\langle \mathbf{r}_i \mathbf{f}_{\rm st}_i \rangle = 0$, so that the virial

$$\sum_{k=1}^{\infty} \langle \mathbf{r}_i \mathbf{f}_{Li} \rangle = -\gamma \sum_{k=1}^{\infty} \langle \mathbf{r}_i \dot{\mathbf{r}}_i \rangle + \sum_{k=1}^{\infty} \langle \mathbf{r}_i \mathbf{f}_{st} \rangle = 0.$$
 (36)

vanishes exactly.

Next, consider the case of a strongly coupled system, $\Gamma \to \infty$, for which we use again the ion sphere model (Sec. II A). Now the ion equation of motion includes the electrostatic force $\mathbf{f} = -\mathbf{r}$: $\ddot{\mathbf{r}} = -\mathbf{r} - \gamma \dot{\mathbf{r}} + \mathbf{f}_{\rm st}$, where we omit subscripts. In contrast to the case of ideal gas treated above, an ion in a strongly coupled system is involved in the Ornstein–Uhlenbeck process in its microscopic sphere, so that $\langle \mathbf{r}\dot{\mathbf{r}} \rangle = (1/2)d \langle r^2 \rangle/dt = 0$, and therefore, $\langle \mathbf{r}\ddot{\mathbf{r}} \rangle = -\langle v^2 \rangle$. We calculate the dot product of both sides of the ion equation of motion and \mathbf{r} . With due regard for the equality $\langle v^2 \rangle = \langle r^2 \rangle$ valid at equilibrium, we derive the same result as above: $\mathbf{rf}_L = 0$ [62].

In the intermediate case of moderate Γ , the ion is involved in both the Brownian and Ornstein–Uhlenbeck process, i.e., its motion is characterized by two time scales. Such process is quite similar to that observed in study [68]. Test runs showed that irrespective of Γ , all results were absolutely insensitive to the choice of γ , which confirms the conclusions made above (note that

Table I. Parameters of the MD simulation for BOCP at different Γ 's. Given are the time integration step τ , the range of ion numbers N, and the range of respective time step numbers N_{τ} (sample sizes are given in parenthesis).

Γ	au	Range of N	Range of $10^4 N_{\tau}$
0.03	0.001	5000-50000	570(286)-6.67(3.33)
0.1	0.002	2500 - 50000	1800(900)-6.67(3.33)
0.3	0.01	2500 – 50000	1800(900)-6.67(3.33)
1	0.01	2500 – 50000	1800(900)-6.67(3.33)
3	0.01	2500 - 50000	1800(900)-6.67(3.33)
10	0.01	2500 – 50000	1800(900)-6.67(3.33)
17	0.01	2500 – 50000	1800(900)-6.67(3.33)
30	0.01	2500 – 50000	1800(900)-6.67(3.33)
100	0.01	2500 – 50000	1800(900)-6.67(3.33)
174	0.05	2500 – 50000	1800(900)-6.67(3.33)
176	0.05	2500 – 50000	1800(900)-6.67(3.33)
178	0.05	2500 – 50000	3600(900)-13.4(3.33)
182	0.05	2500 – 50000	3600(900)-13.4(3.33)
190	0.05	2500 – 50000	3600(900)-13.4(3.33)
200	0.05	2500 - 10000	3600(900) - 304(76.0)
210	0.05	2500 - 10000	3600(900) - 304(76.0)
300	0.05	2500 – 50000	5400(900)-20.0(3.33)
650	0.1	2500 – 21200	5400(900) - 109(18.2)
1000	0.1	2500-30000	5400(900)-54.9(9.2)
	<u> </u>	<u> </u>	

it must be true solely at equilibrium). For all BOCP simulations, we borrowed $\gamma \simeq 0.09$ from earlier studies [20, 62, 64].

We apply the specular reflection boundary conditions for the equation of motion (29), i.e., when an ion crosses the surface of a sphere of the radius R_b then its velocity \mathbf{v}_i is transformed as

$$\mathbf{v}_i' = \mathbf{v}_i - \frac{2\mathbf{r}_i \mathbf{v}_i}{r_i^2} \mathbf{r}_i. \tag{37}$$

Due to finiteness of the time integration step, the ion velocity can be transformed only at the point where $r_i > R_b$, i.e., the ion density distribution $f_c(r)$ is never sigmoid-shaped but its vanishing at $r \gtrsim R_b$ is smooth. Hence, if we would set $R_b = R$ then some artificial charged layer was formed beyond the surface of compensating background, which leads to violation of the charge neutrality inside BOCP. This effect cannot be eliminated completely but it can be minimized if R_b coincides with the ion equimolar radius. Since the average distance at which an ion propagates during the time τ is $\tau/\sqrt{2\pi\Gamma}$, the shift $R_b = R - \tau / \sqrt{8\pi\Gamma}$ minimizes the boundary effect. Note that variation of such shift by several times does not change the results principally but it increases significantly the smallest size beginning from which the size dependence $u(\Gamma)$ conforms to Eq. (19) thus indicating the increase of the surface effect. Additionally, at each time step, the ion velocity was normalized to $\sqrt{2/\Gamma}$ if it exceeded $\sqrt{25/\Gamma}$.

The choice of time integration step depends on Γ , and $\tau(\Gamma)$ is an increasing function due to slow-down of the thermal motion. If τ is too small then too large num-

ber of time steps N_{τ} that exceeds the computational resources is required to equilibrate the system. For too large τ , the accuracy of the used numerical integration scheme becomes insufficient, which results in noticeable errors in determined parameters. Thus, an optimum τ was determined for each Γ from the condition that the determined parameters are almost insensitive to variation of τ by several times (Table I).

MD simulation of BOCP was performed for the set of BOCP sizes N = 2500, 3540, 5000, 7070, 10000, 14000,21200, 30000, and 50000 at different Γ . Due to limitation of computational resources, the maximum N is defined by the minimum N_{τ} , for which variation of the determined quantity is much less than its estimated error. Hence, in some cases, simulations were performed in a limited range of N. The ranges of N and N_{τ} estimated in such a way for different Γ 's are also listed in Table I. For the sizes within the range limits, $N_{\tau} \propto N^{-2}$. The upper bound of N at $\Gamma = 200$ and 210 is a consequence of higher fluctuations in the system, where a transitional regime from fluid to solid (fluid core and solid shells) takes place. At $\Gamma = 650$ and 1000, the BOCP equilibration time is sharply increased due to the decrease in the ion self-diffusion coefficient for a solid system. For $\Gamma = 0.03$, the lower bound of N is due to the fact that the size dependence $u(\Gamma)$ does not conform to Eq. (19) at N < 3540.

First, the positions of N ions were initialized by the homogeneous random spatial distribution in a sphere of the radius R_b . Then Eqs. (29) were integrated numerically using the Verlet algorithm. After the relaxation of the system to equilibrium state after $N_\tau/2$ time steps, data were collected every 100 time steps. For the calculation of $f_p(r)$ (7), an ion closest to the BOCP center was selected with the same time interval. The data for different quantities were averaged, and the error was estimated specifically for each quantity (Sec. IIIB). Eventually, obtained data were used for determination of the OCP properties in the thermodynamic limit.

B. Simulation results

Figure 1 shows typical ion density distributions and the radial distribution functions obtained in our simulations. Largely, in the BOCP core region, the radial distribution functions are almost identical to those obtained for OCP in various MC simulations starting from [40] (Fig. 1b). Namely, a dip in $f_p(r)$ at small distances for $\Gamma = 0.1$ is indicative of repulsion, the radial distribution function exhibits two maxima indicating a smooth transfer from the gaslike to fluid state at $\Gamma = 30$, and several maxima emerge at $\Gamma = 200$, which is somewhat below the melting point for the size N = 5000. The maxima at larger r are due to the shells formed closer to the BOCP boundary (two shells can be seen already at $\Gamma = 30$). Note that melting of shells is observed at $\Gamma = 60-90$ well below the melting point of a central part of the Coulomb clusters [64]. In Fig. 1a, the ion density distribution $f_c(r)$ demonstrates qualitatively the same regularities: in most of the BOCP volume, the ions are homogeneously distributed at $\Gamma=0.1$ and 30, although two shells are visible for $\Gamma=30$. However, the curve for $\Gamma=200$ is more indicative of the shell structure than in Fig. 1b because in the latter, departure of the ion, for which $f_p(r)$ is determined, from the BOCP center smooths the peaks of shells considerably. Instead, as follows from Fig. 1a, shells fill a significant part of the BOCP volume at high Γ . As is seen in Fig. 1c, both $f_p(r)$ and $f_c(r)$ show behavior with irregular tooth-shaped peaks typical for a solid.

The size dependence of $u(\Gamma, N)$ obtained from MD simulation is illustrated by Fig. 2a, which testifies the accuracy of its approximation by the function (19). Indeed, the actual deviation of this approximation from the obtained MD results for all BOCP sizes, e.g., for $\Gamma = 30$, varies from 4×10^{-8} to 8×10^{-6} . The accuracy of MD results determined by a standard statistical method depending on the sample size is of the same order of magnitude and principally it can be further decreased by the increase in N_{τ} . However, the difference in $u(\Gamma, N)$ obtained for two similar runs initialized with different random seeds is orders of magnitude greater, which means that a real simulation error is of physical nature. Thus, this difference may be due to the low-frequency non-vanishing wing of the phonon spectrum when the inverse phonon frequency is of the same order as τN_{τ} , or it may arise from different structures of the polycrystal formed at $\Gamma \gg 1$. Thus, for each Γ and N, the simulation was repeated twice; $u(\Gamma, N)$ was then estimated as the average of these two results while the accuracy was set to the modulus of their difference. For, $\Gamma = 30$, such accuracy does not exceed 4×10^{-5} , which is noticeably greater than the accuracy of data approximation. The same procedure was applied for all determined sizedependent quantities. It is this accuracy that is shown by error bars in Figs. 2, 4, and 6–8. Note that in most figures, the error bar width is less than the dot marker

Albeit the function (19) approximates $u(\Gamma, N)$ with a high accuracy, the size dependence is very weak at great N. This makes problematic extrapolation of $u(\Gamma, N)$ to the thermodynamic limit. In other terms, it is necessary to estimate the accuracy of $u_{\infty}(\Gamma)$ obtained from such extrapolation. To this end, from the set of data for the same Γ , we selected at random two triplets of unmatched BOCP sizes N and fitted (19) to these triplets. Modulus of the half-difference between two values of $u_{\infty}(\Gamma)$ obtained in such a way is associated with the accuracy of its determination in Figs. 3 and 5. As is seen in Table II, the overall relative accuracy of extrapolated quantities is of the order of 0.1%, which is greater than the errors for individual values but still reasonably good. Figure 2b illustrates an extremely slow convergence of $u(\Gamma, N)$ to $u_{\infty}(\Gamma)$. As is seen, the accuracy of 1% is reached already for N = 45000, which is close to the size used in this work, while the overall approximation accuracy of 0.1% is attained only for $N = 10^{34}$, i.e., for a large body.

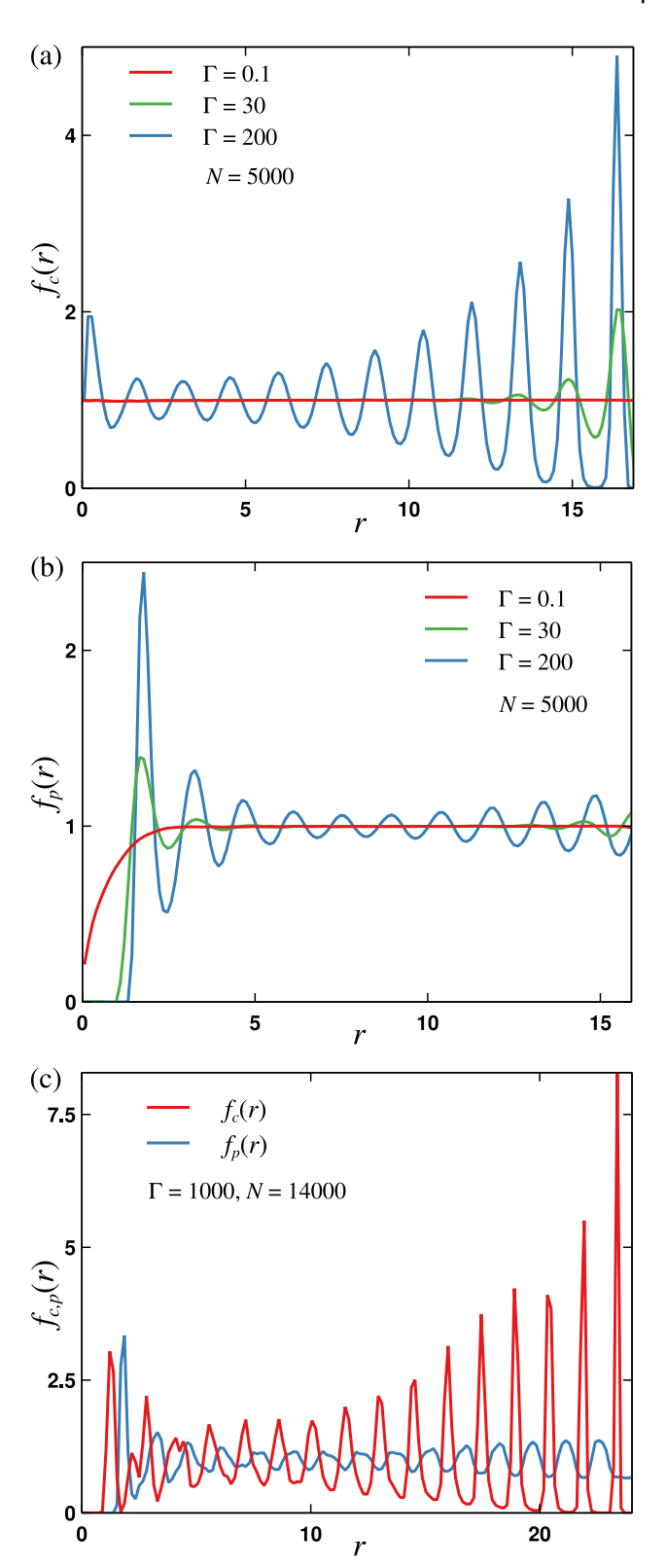


Figure 1. Ion density distribution $f_c(r)$ (8) and the radial distribution function $f_p(r)$ (7) of BOCP at different Γ : (a) and (b) $\Gamma=0.1$, 30, and 200 (red, green, and blue lines, respectively), N=5000; (c) $f_c(r)$ (red line) and $f_p(r)$ (blue line) at $\Gamma=1000$ and N=14000.

Table II. BOCP parameters in the thermodynamic limit. Listed are the total potential energy u_{∞} and its fit (38), (39); the excess energy of interionic interaction u_{pex} , the excess energy of interaction between the ions and background u_{bex} , and the shifted ion compressibility factor $Z_i - 1$ calculated from the excess energies (16) and virial (24) (for u_{pex} and u_{bex} , the results for N = 21200 are listed).

Γ	u_{∞}	$u_{ m fit}$	$u_{p\mathrm{ex}}$	$u_{b\mathrm{ex}}$	$Z_i - 1$ (energy)	$Z_i - 1$ (virial)
0.03	-0.1466 ± 0.0027	_	-0.1402 ± 0.0093	-0.0059 ± 0.018	-0.00157 ± 0.0002	-0.00143 ± 0.001
0.1	-0.2659 ± 0.0025	-0.2659	-0.2391 ± 0.0151	-0.0261 ± 0.030	-0.00779 ± 0.0002	-0.00798 ± 0.001
0.3	-0.4050 ± 0.0050	-0.4050	-0.3726 ± 0.0010	-0.0409 ± 0.002	-0.0332 ± 0.0001	-0.0343 ± 0.0005
1	-0.5785 ± 0.0016	-0.5784	-0.5095 ± 0.0002	-0.1139 ± 0.0004	-0.1317 ± 0.0004	-0.1320 ± 0.0008
3	-0.7109 ± 0.0005	-0.7111	-0.5941 ± 0.00002	-0.2113 ± 0.00002	-0.3834 ± 0.0004	-0.3853 ± 0.0011
10	-0.8044 ± 0.0012	-0.8041	-0.6132 ± 0.00008	-0.3665 ± 0.0002	-0.8241 ± 0.0008	-0.8242 ± 0.0018
17	-0.8304 ± 0.0001	-0.8302	-0.6056 ± 0.00009	-0.4375 ± 0.0002	-0.9531 ± 0.0004	-0.9443 ± 0.0057
30	-0.8506 ± 0.0002	-0.8507	-0.5975 ± 0.00003	-0.4978 ± 0.00004	-0.9954 ± 0.0006	-0.9988 ± 0.0026
100	-0.8762 ± 0.0010	-0.8765	-0.5930 ± 0.00004	-0.5630 ± 0.00008	-0.9976 ± 0.0010	-0.9851 ± 0.0070
174	-0.8834 ± 0.0001	-0.8831	-0.5939 ± 0.00002	-0.5766 ± 0.00002	-0.9984 ± 0.0013	-1.0027 ± 0.0039
176	-0.8835 ± 0.0001	-0.8833	-0.5939 ± 0.00001	-0.5768 ± 0.00001	-0.9997 ± 0.0007	-0.9984 ± 0.0020
178	-0.8841 ± 0.0002	-0.8866	-0.5939 ± 0.020	-0.5771 ± 0.051	-0.9982 ± 0.0012	-0.9951 ± 0.0038
182	-0.8850 ± 0.0002	-0.8869	_	_	-0.9973 ± 0.0015	-0.9961 ± 0.0018
190	-0.8881 ± 0.0007	-0.8874	_	_	-0.9983 ± 0.0016	-0.9955 ± 0.0022
200	-0.8913 ± 0.0045	-0.8879	_	_	-0.9992 ± 0.0011	-0.9940 ± 0.0036
210	-0.8950 ± 0.0025	-0.8883	_	_	-0.9984 ± 0.0005	-0.9959 ± 0.0016
300	-0.8909 ± 0.0009	-0.8909	-0.5958 ± 0.00001	-0.5859 ± 0.00002	-0.9992 ± 0.0012	-0.9994 ± 0.0094
650	-0.8939 ± 0.0012	-0.8939	-0.5958 ± 0.00002	-0.5912 ± 0.00002	-0.9947 ± 0.0022	-0.9860 ± 0.0068
1000	-0.8948 ± 0.0002	-0.8948	-0.5958 ± 0.00001	-0.5928 ± 0.00005	-0.9949 ± 0.0029	-1.0134 ± 0.0126

The total electrostatic energy $u_{\infty}(\Gamma)$ determined from MD simulation is listed in Table II. These data were fitted by the function borrowed from [45]:

$$\Gamma u_{\text{fit}} = A + B\Gamma + C\Gamma^s + D\Gamma^{-s}, \quad 0.1 \le \Gamma \le 174, \quad (38)$$

with A = -0.8304212370, B = -0.8974963531, C = 0.9500252063, D = 0.19951975244, and s = 0.2396352836, and by the theoretical dependence (cf. (25) and (26))

$$u_{\rm fit} = \beta_0 + \frac{\beta_1}{\Gamma} + \frac{\beta_2}{\Gamma^2}, \quad 174 < \Gamma \le 1000$$
 (39)

with $\beta_0 = -0.8963837125$, $\beta_1 = 1.5311038492$, and $\beta_2 = 35.092640432$. Note that at $\Gamma \leq 176$, $|u_{\infty} - u_{\rm fit}| \sim 10^{-4}$, which is much less than the error in u_{∞} definition.

The parameters in Eq. (39) obtained from the fitting procedure prove to be close to those calculated in the harmonic lattice approximation: $\beta_0 \approx u_0$ with the same accuracy of $\sim 10^{-3}$ as in Table II and $\beta_1 \approx 3/2$. The first anharmonicity correction coefficient turns out to be of the same order of magnitude as calculated in study by Chugunov and Baiko [26] for the classical OCP, $\beta_2 \approx 10.58$. Apparently, the accuracy of β_2 determination could be enhanced if more points were calculated in the interval $174 < \Gamma \le 1000$ (at present, only three were fitted), and it might bring our result closer to [26].

Determined energies are compared with the results of different studies in Fig. 3. As is seen, they are in a good agreement with early data by Brush *et al.* [40] and Hansen [41], however, dispersion of these data are much greater than the accuracy attained in this work. Note that here, our error bars are smaller than the dot

marker sizes. The results obtained later by Slattery et al. [43] are in perfect agreement with modern data from the works by Demyanov and Levashov [47], and by Caillol [45] and Caillol and Gilles [46] for $\Gamma \leq 1$, while at $\Gamma > 1$, the data from [46] are situated higher than any other data. At $\Gamma < 0.1$, our results scarcely deviate from the Debye-Hückel approximation, while the data from [46] are noticeably higher. At $\Gamma > 174$, our data reach asymptotically the bcc energy u_0 , and in this region, they are in a very good agreement with [43] (Fig. 5). At the same time, for $0.1 < \Gamma < 174$, our energies are appreciably lower than other data, which can be clearly seen in the inset in Fig. 3. Here, a typical difference is about 0.5\%, which is much higher than the declared accuracy of all results. Apparently, this difference may arise from the limitation on system microscopic states imposed by the PBC, which can be qualitatively treated as strong correlations between the particles in a supercell and its images. Since the characteristic decay length of the Ewald potential is of the order of the simulation cell length, the resulting long-range interaction may contribute noticeably to the total system energy. In contrast, BOCP does not have such limitation, and this leads the system to a more favorable state. However, at $\Gamma \to \infty$, the system occupies a single state, which results in convergence of [43] and our data.

Based on Eqs. (38) and 39), we can approximate the internal energy in a wide range of Γ in the form

$$\varepsilon_{iex}(\Gamma) = \begin{cases} u_{fit}(\Gamma) - u_0, & 0.1 \le \Gamma \le \Gamma_{m}, \\ \frac{3}{2\Gamma} + \frac{\beta_2}{\Gamma^2}, & \Gamma > \Gamma_{m}, \end{cases}$$
(40)

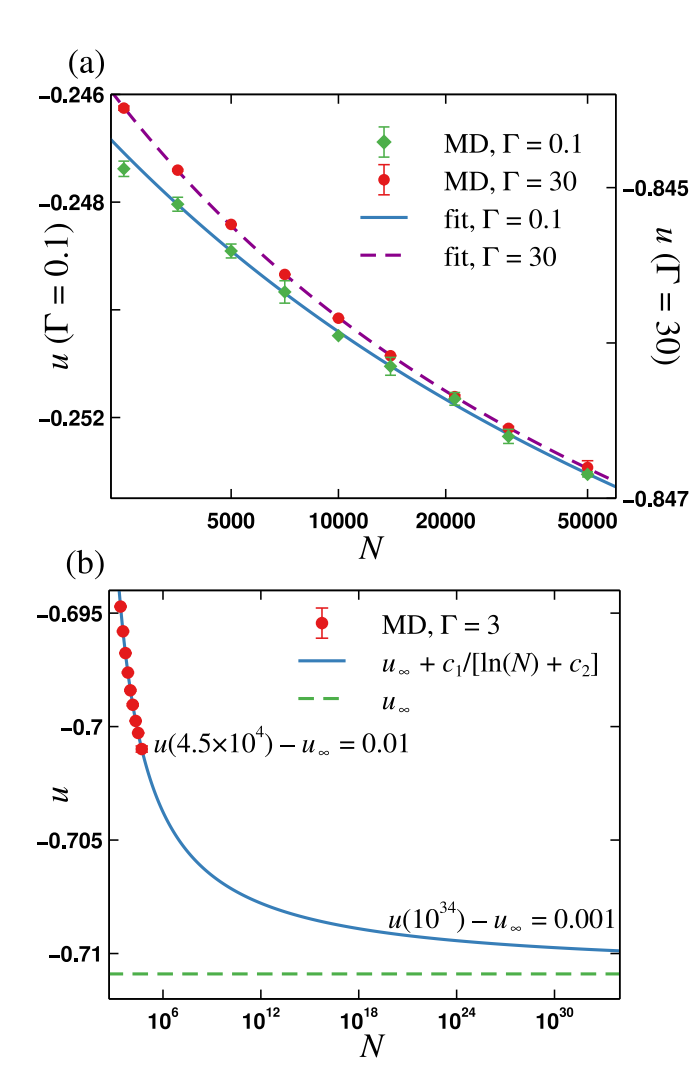


Figure 2. Size dependence of the BOCP total electrostatic energy from MD simulation (dots) and its fit by Eq. (19) (lines): (a) diamonds and solid lines correspond to $\Gamma=0.1$ and circles and dashed line, to $\Gamma=30$; (b) circles indicate MD data for $\Gamma=3$, solid line is their fit, and dashed line marks the thermodynamic limit $u_{\infty}(3)$.

and the Helmholtz free energy, as

$$f_{iex}(\Gamma) = \int \frac{\varepsilon_{iex}(\Gamma)}{\Gamma} d\Gamma$$

$$= \begin{cases} \omega_{1}(\Gamma) + \Delta\omega_{1}, & 0.1 \leq \Gamma \leq \Gamma_{m}, \\ \omega_{2}(\Gamma), & \Gamma > \Gamma_{m}, \end{cases}$$
(41)

where

$$\omega_1(\Gamma) = (B - u_0) \ln \Gamma - \frac{A}{\Gamma} + \frac{C\Gamma^{s-1}}{s-1} - \frac{D\Gamma^{-s-1}}{s+1}, (42)$$

 $\omega_2(\Gamma) = -\beta_1/\Gamma - \beta_2/2\Gamma^2$, $\Delta\omega_1 = \omega_2(\Gamma_{\rm m}) - \omega_1(\Gamma_{\rm m})$, and we take into account that $f_{iex}(\Gamma)$ is a continuous function at $\Gamma = \Gamma_{\rm m}$.

A good parameter for investigation of melting is the thermal fraction of the Coulomb energy $\Gamma[u(\Gamma, N) - u_0]$

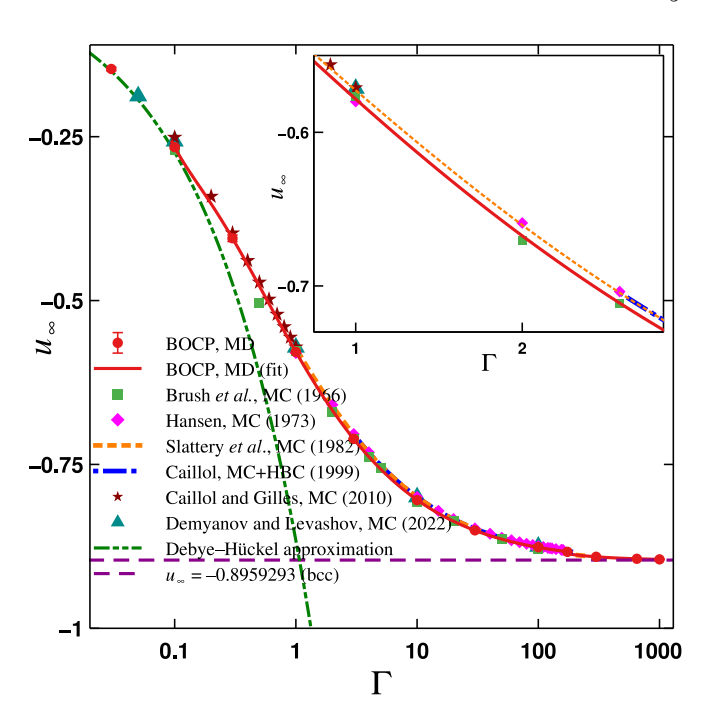


Figure 3. Thermodynamic limit of the BOCP electrostatic energy compared with the results of MC simulations for the OCP with PBC. MD results of this work (circles) and their approximation by the functions (38) and (39) (solid line), MC results by Brush et al. [40] (squares), Hansen [41] (diamonds), Caillol and Gilles [46] (stars), Demyanov and Levashov [47] (triangles). Approximation of the results available in studies by Slattery et al. [43] and Caillol (MC within hyperspherical boundary conditions) [45] are shown by dotted and dashed-dotted lines, respectively. Dashed-dotted-dotted line indicates the Debye–Hückel approximation and dashed line, the Madelung constant for bcc lattice. Inset shows a magnified fragment of this figure.

[43]. It is well known that, in contrast to the bulk system, phase transitions in finite-size systems are very diffuse, both in temperature and phase composition. As can be seen in Fig. 4, BOCP is not exclusion. In this case, melting can be associated with the Coulomb coupling parameter $\Gamma_{\rm m}$ corresponding to the maximum of $\Gamma_{\mathrm{m}}[u(\Gamma_{\mathrm{m}},N)-u_{0}].$ This maximum is shifted toward lower values with the increase in N. Inset shows fitting $\Gamma_{\rm m}$ with the exponential decay function $\Gamma_{\rm m}(N) = 174.0 +$ $647.995 \exp(-N/1729.886)$, from which the estimate for the bulk melting parameter is $\Gamma_{\rm m}(\infty)=174\pm2$. The accuracy of 2 corresponds to the error of maximum resolution for the size-dependent function $\Gamma_{\rm m}[u(\Gamma_{\rm m},N)-u_0]$ due to the error in $u(\Gamma, N)$. Obtained value correlates with that obtained in [43] ($\Gamma_{\rm m}=178$) and coincides with the results by Ichimaru [2], Dubin and O'Neil [14] and Khrapak and Khrapak [39]. The absence of appreciable metastable region in the neighborhood of $\Gamma_{\rm m}$ is noteworthy. It means that the fluid-solid transition is very fast, at least, its characteristic time is less than N_{τ} . This can be connected with the solid-like shells near the BOCP boundary, which initiate crystallization propagating to

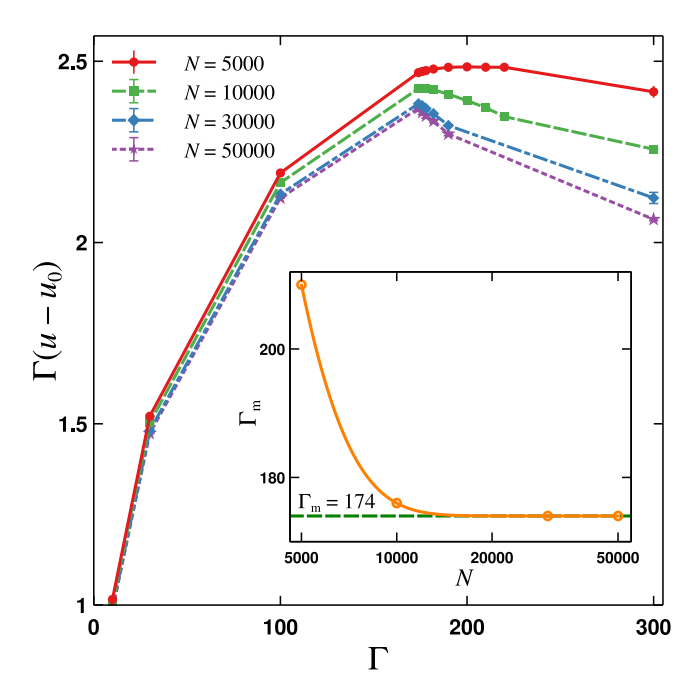


Figure 4. Thermal fraction of the BOCP electrostatic energy as a function of Γ for the BOCP size N=5000 (solid line), 10000 (dashed line), 30000 (dashed-dotted line), and 50000 (dotted line). Inset shows the size-dependent Coulomb coupling parameter $\Gamma_{\rm m}(N)$ (open circles); solid line indicates the curve fit and dashed line, the thermodynamic limit $\Gamma_{\rm m}(\infty)$.

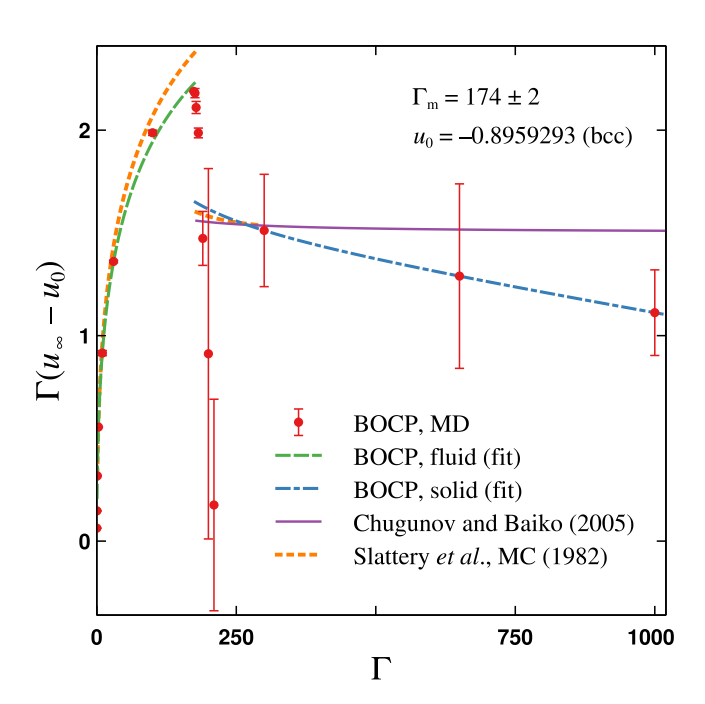


Figure 5. Thermal fraction of the electrostatic energy in the thermodynamic limit as a function of Γ . This work: MD results (dots) and their approximation by the function (38) (dashed line) and (39) (dashed-dotted line). Solid line indicates calculations based on the harmonic lattice approximation [26] and dotted line, MC results [43].

the BOCP center.

Another way to estimate $\Gamma_{\rm m}$ is based on the parameter $\Gamma(u_{\infty}-u_0)$ for the bulk fluid and solid (Fig. 5). Here, in contrast to Fig. 4, the dependence of this parameter on Γ forms a cliff at $\Gamma_{\rm m}$ = 174 \pm 2, where again, the estimation for accuracy follows from the error in $u_{\infty}(\Gamma, N)$. Note that at $190 \le \Gamma \le 210$, the dots are situated well below the data for $\Gamma \geq 300$. This is a consequence of a bad applicability of the principal size dependence (19) for N > 10000, so that the data in Table II were obtained only for the smaller sizes. Very large errors of u_{∞} definition in this range of Γ are indicative of enormous fluctuations of the BOCP structure at $\Gamma \approx \Gamma_{\rm m}$. Here, N_{τ} 's limited by the computational resources and listed in Table I seem to be insufficient to reach equilibration for such sizes. However, one can testify that at high Γ , our data agree qualitatively with the analytical results by Chugunov and Baiko [26]. Note that, as for a finite size BOCP, we have found no metastable region. In addition, it is worth mentioning that the excess free energy at the melting point (28) amounts to 0.0092002, which proves to be an order of magnitude less than what follows from the estimate of free energy in [43].

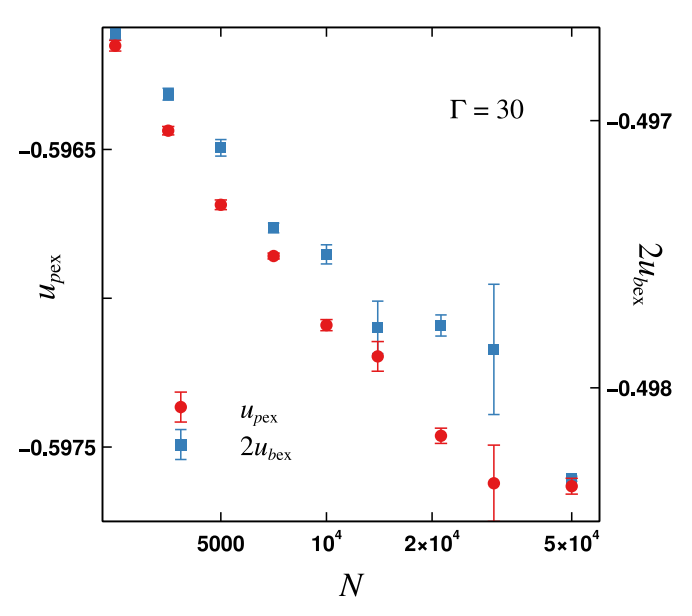


Figure 6. Size dependences of the excess interatomic electrostatic energy u_{pex} (circles) and the excess ion–background electrostatic energy u_{bex} (squares) at $\Gamma = 30$.

Now turn to determination of the excess interatomic electrostatic energy and the excess ion–background electrostatic energy (Table II and Fig. 6). The size dependences of excess energies $u_{pex}(\Gamma, N)$ and $u_{bex}(\Gamma, N)$ (5) determined in our simulation reveal an overall trend to decrease with the increase in N. However, the decrease is so small that we failed to assign any functional dependence to it in the investigated range of system parameters. Rigorously speaking, we are not able to extrapolate the results to the thermodynamic limit due to an extremely narrow abscissa range in Fig. 6 and hence,

confine ourselves to its estimate by taking these quantities for N = 21200. Here, the corresponding errors were calculated in the same way as for $u(\Gamma, N)$. The resulting dependences $u_{pex}(\Gamma)$ and $u_{bex}(\Gamma)$ are shown in Fig. 7 and Table II. Since at $182 \le \Gamma \le 210$, BOCP of the sizes N > 10000 were not simulated, the corresponding u_{pex} and u_{bex} are not listed in table. Behavior of these dependences is in agreement with the asymptotic analytical predictions (12) and (18), which is indicative of the fact that Fig. 7 represents a satisfactory estimate for the investigated quantities in the thermodynamic limit. One can see that as Γ is decreased, $u_{bex}(\Gamma)$ vanishes more rapidly, which can be explained by the difference in $f_p(r)$ (7) and $f_c(r)$ (8). Indeed, at $\Gamma = 0.1$, $f_c \approx 1$ (Fig. 1a), which vanishes the integral (10), whereas f_p is noticeably different from zero at short distances (Fig. 1b) resulting in nonzero $u_{pex}(\Gamma)$ (9). Since (9) and (10) were written in the approximation of pair correlations for a homogeneous medium, it is clear that such approximation is ineffective for $u_{bex}(\Gamma)$, whose analytical calculation would require the inclusion of higher-order correlations. In this connection, a fast decrease of $u_{bex}(\Gamma)$ at $\Gamma > 0.3$ is indicative of inadequacy of the pair correlations approximation, and therefore, $\Gamma = 0.3$ can be regarded as an upper bound for the Debye-Hückel approximation or the weakly coupled regime. Notably, it follows from the recent analysis [55] of the reduced coefficients of self-diffusion, shear viscosity, and thermal conductivity of OCP based on the Debye-Hückel plus hole approach [51] that the binary collision approaches break down at $\Gamma > 0.3$, when OCP is no more a weakly coupled system.

At high Γ , $u_{pex}(\Gamma)$ reaches a solid state value already at $\Gamma=30$ while $u_{bex}(\Gamma)$, only at $\Gamma=650$, which is indicative of strong ionic correlations in this region. Interestingly, $u_{bex}(\Gamma)$ has a shallow minimum at $\Gamma\approx 10$, which coincides with a gas-to-liquid dynamical crossover in OCP discussed in works [21] and [54], so this minimum can serve as yet another definition of the Frenkel line in OCP.

Determination of the energies $u_{pex}(\Gamma, N)$ and $u_{bex}(\Gamma, N)$ makes it possible to obtain the ionic compressibility factor (16) In Fig. 8, it is compared with the same quantity estimated from the virial (24). It is noteworthy that (i) estimates from the energies are in a good agreement with those from virial, however, the latter have much larger scatter and (ii) within the accuracy attained in our simulation, Z_i seems to be sizeindependent. Such peculiarities hold true irrespective of Γ . Thus, we take the average of all Z_i available for different N at the same Γ as an estimate of its thermodynamic limit, the error being calculated by application of a standard statistical method to the sample of the size up to 9. The resulting dependence $Z_i(\Gamma)$ is shown in Fig. 9. As is seen, the results from energy and virial are hardly distinguishable, except for the highest Γ , which validates correctness of Z_i determination. At $\Gamma < 0.3$, the obtained Z_i almost coincides with the ionic compressibility factor $1 - \Gamma^{3/2}/2\sqrt{3}$ that results from the

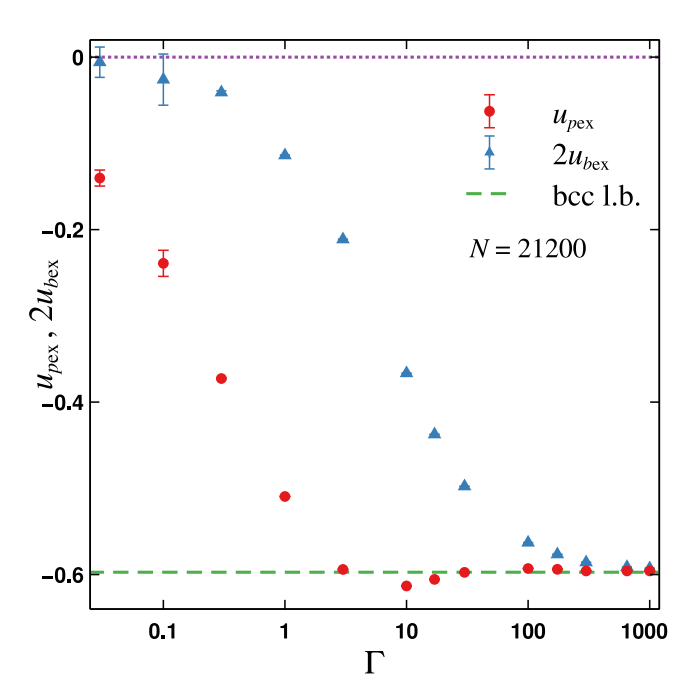


Figure 7. Excess interatomic electrostatic energy (circles) and the excess ion–background electrostatic energy (triangles) as functions of Γ . Dashed line indicates the bcc lower bound for these quantities; N=21200.

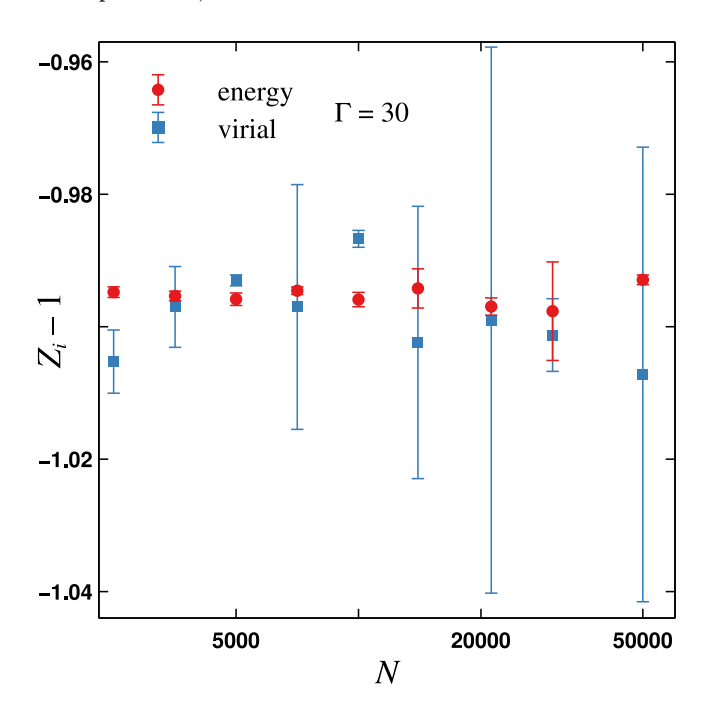


Figure 8. Size dependence of the ionic compressibility factor Z_i determined from MD simulation using Eqs. (16) (circles) and (24) (squares) at $\Gamma = 30$.

Debye–Hückel approximation, as it must. In the interval $0.1 \le \Gamma \le 30$, Z_i can be approximated by the function

$$Z_i(\Gamma) = c_1 + c_2 \tanh\left(\frac{c_3 - \ln \Gamma}{c_4}\right),$$
 (43)

with $c_1=0.4613762483$, $c_2=0.5260100823$, $c_3=1.4830111629$, and $c_4=1.3508409652$. Note that at $\Gamma>30$, $Z_i\simeq 0$ as it follows from Eq. (13), and in the entire range of Γ , $Z_i>0$. Note that at $\Gamma>300$, images of the cold ions from a spherical boundary are so rare that they can be neglected. Therefore, the difference between BOCP and Coulomb cluster diminishes, and for these systems, Z_i must coincide. In [62], a negative value $Z_i=-0.04\pm0.06$ was obtained at $\Gamma=500$ as a result of the substantial simulation inaccuracy.

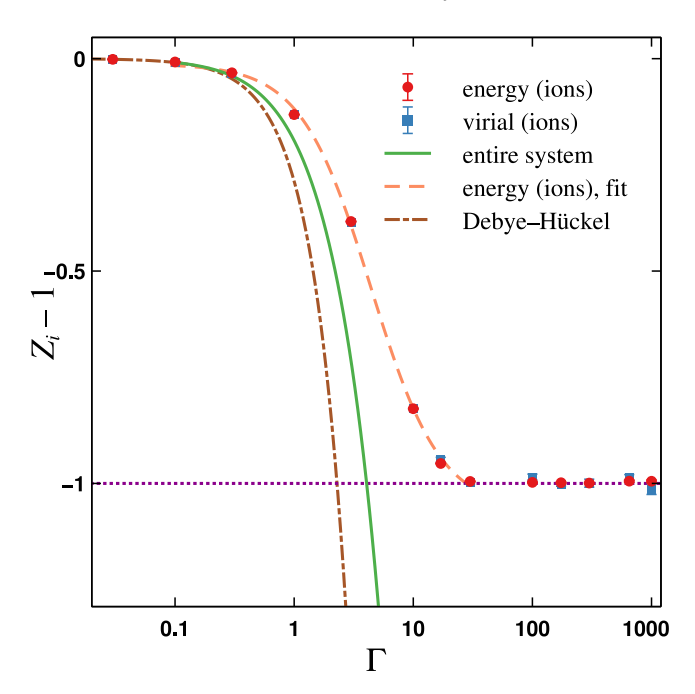


Figure 9. Ionic compressibility factor Z_i determined from MD simulation using Eqs. (16) (circles) and (24) (squares). Dashed curve indicates the approximation (43) of Z_i from energies; solid line, Z_i for the entire system (21); and the dashed-dotted line, Z_i in the Debye–Hückel approximation.

IV. APPLICATION TO LAMMPS

A. Simulation procedure

A common way to calculate properties of an OCP system is to use the Ewald potential, which is typically split into two parts: $\operatorname{erfc}(\alpha r)/r$, dominant at short and medium distances within the simulation cell, and $\operatorname{erf}(\alpha r)/r$, a smooth, long-range function treated in reciprocal space. Here, α is the Ewald damping (splitting) parameter, chosen such that the real-space contribution at the cutoff length r_c satisfies the condition $\operatorname{erfc}(\alpha r_c)/r_c \lesssim \varepsilon_0$, where ε_0 is the target relative error for forces. Interactions within r_c are calculated directly in real space, while interactions beyond r_c are included via the reciprocal-space sum over periodic images. It is assumed that thermodynamic properties of the system

are effectively independent of the precise cutoff, as long as α and r_c are chosen to meet the desired accuracy ε_0 .

To examine the effect of the cutoff length on derived thermodynamic quantities arising from specific computational algorithms, we performed a series of MD simulations using the stable release of LAMMPS (29 August 2024) [69], compiled with the ScaFaCoS library v1.0.4 [70].

The total number of particles N was fixed within each simulation, but varied between different simulations and the exact values will be specified later. Periodic boundary conditions were applied in all three directions of a cubic cell with the edge length $L = (4\pi N/3)^{1/3}$. The integration time step was chosen to be dependent on the Coulomb coupling parameter Γ as $\tau = 10^{-3}(0.2\Gamma + 2)$.

Ions of mass m=1 bearing the charge z=1 and atom style charge were initialized randomly for fluid simulations and as a bcc lattice for solid-state simulations. Initial velocities were assigned the Maxwellian distribution corresponding to temperature $T=1/\Gamma$. In both cases, the pair style coul/long was used with the cutoff length r_c . Long-range interactions were handled with the k-space solver ewald for simulations employing the Ewald potential [58], or with pppm for simulations using the PPPM method [67], in both cases with the target relative accuracy $\varepsilon_0=10^{-6}$.

All simulations were carried out in the microcanonical ensemble. During the initial 5×10^6 time steps, the Langevin thermostat with damping parameter 0.5 was applied. The thermostat was then disabled, and the system was allowed to evolve freely for at least 5×10^6 additional time steps, while data were collected every 100 steps. The reported results were obtained by averaging over the final quarter of each trajectory.

B. Effect of the ionic pressure

In order to demonstrate the dependence of ionic compressibility factor of a system on chosen cutoff length with fixed relative error, a series of MD simulations were performed under simulation conditions specified in Sec. IV A, while the total number of ions was chosen to be $N=10^3$ and k-space style pppm was used.

The ion compressibility factor Z_i shows a strong dependence on the cutoff length r_c , as illustrated in Fig. 10, and this dependence becomes stronger with the increase in Γ (cf. [63]). In all cases, Z_i grows as r_c increases, indicating that the virial is also sensitive to r_c . For weak coupling ($\Gamma = 0.1$), Z_i varies only slightly with r_c and stays close to the BOCP reference value, demonstrating that the effect is present but relatively modest. At intermediate coupling ($\Gamma = 10$), the growth of Z_i with r_c becomes clearly visible though still moderate. In the strongly coupled regimes ($\Gamma = 160$ and $\Gamma = 200$), the dependence turns dramatic: Z_i rises by orders of magnitude as r_c increases. Thus, ionic compressibility factor increases with increasing cutoff distance regardless

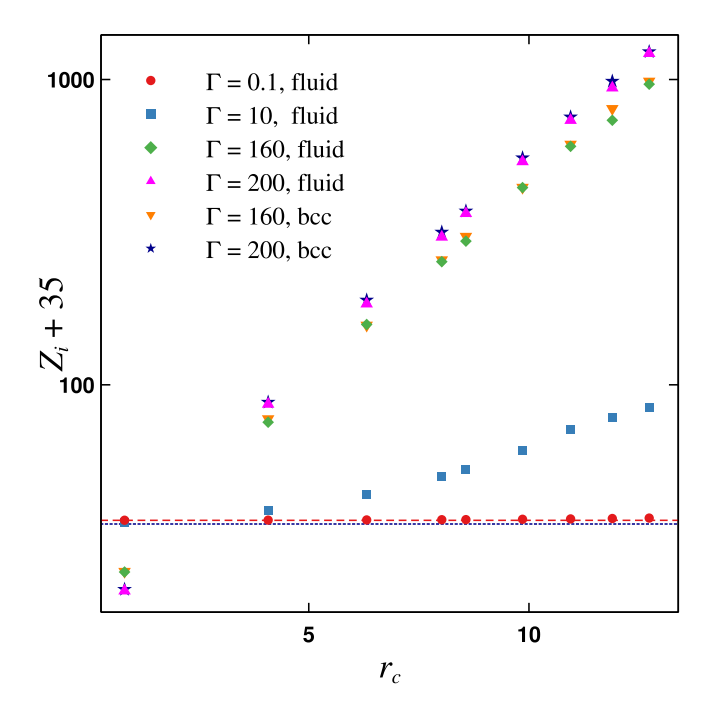


Figure 10. Ionic compressibility factor Z_i for OCP as a function of the LAMMPS cutoff length r_c for the cases of random initialization (fluid) at $\Gamma=0.1$ (circles), $\Gamma=10$ (squares), $\Gamma=160$ (diamonds), and $\Gamma=200$ (triangles up) and initialization as bcc (solid) at $\Gamma=160$ (triangles down) and $\Gamma=200$ (stars). Dashed and dotted lines illustrate Z_i obtained for BOCP at $\Gamma=0.1$ and 200, respectively.

of coupling parameter, however while it is weak but detectable at small Γ , the dependency strengthens steadily at intermediate coupling, and dominates the behavior at strong coupling. The choice of initial configuration (fluid vs. solid) appears to have no decisive influence on the resulting Z_i values.

From a physical perspective, a strong dependence of Z_i on r_c at high Γ reflects the emergence of interfacial effects in condensed states. In this regime, truncation of the Coulomb potential effectively modifies the balance between bulk and surface terms of the virial. The rapid increase of Z_i with r_c can therefore be interpreted as an artifact of introducing a spurious surface tension in a nominally homogeneous system with periodic boundaries. While relatively small in weakly coupled plasmas, this artificial surface term dominates the virial at strong coupling, leading to nonphysical values of Z_i depending on r_c .

In this context, it becomes necessary to determine the proper cutoff length r_c that yields the correct ionic pressure. This was done by numerically solving the equation $Z_{\text{MD}}(r_c) = Z_i(\Gamma)$ at the same Γ for r_c , i.e., by varying r_c in the range from 0.1 to 16 and comparing the resulting Z_{MD} with the BOCP reference value $Z_i(\Gamma)$ (43). In all simulations, the total number of ions was fixed at $N=29^3$, and the ions were initialized randomly, except for the case $\Gamma=300$, where the bcc lattice initialization

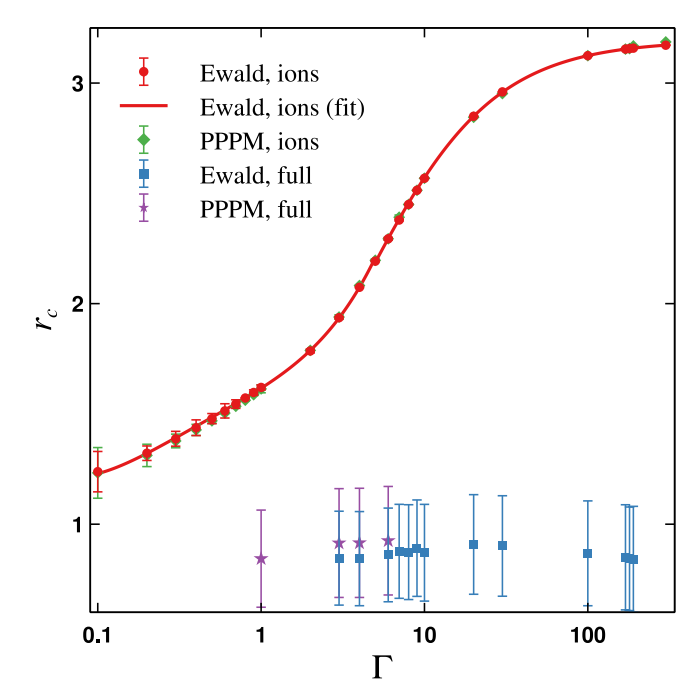


Figure 11. LAMMPS cutoff length r_c ensuring equality of the compressibility factor calculated from the virial for OCP and the ionic compressibility factor of BOCP (43) for the Ewald and PPPM calculation methods (circles and diamonds, respectively), and equality of the compressibility factor calculated from the OCP virial and the OCP potential energy (21) for the Ewald and PPPM calculations (squares and stars, respectively). Solid line is the dependence $r_c(\Gamma)$ (44) and (45) fitting dots.

was used. We also attempted to determine the cutoff r_c that ensures the correct compressibility factor of the entire system, by solving $Z_{\rm MD}(r_c)=Z$ with Z defined by (21). The resulting dependence of the optimal cutoff length r_c on Γ is shown in Fig. 11. For the ionic compressibility factor criterion, the cutoff obtained with the Ewald method exhibits a smooth monotonic increase with Γ approaching $r_c \approx 3$ at strong coupling. The PPPM method follows the same trend and shows no significant deviation from the Ewald results, while reducing the computational cost. The fitted curve is given by the expressions

$$r_c(\Gamma) = a_0 + a_1 \eta + a_2 \eta^2 + a_3 \eta^3 + a_4 \eta^4,$$
 (44)

where $\eta=\ln(\Gamma),\ a_0=1.616474,\ a_1=0.205984,\ a_2=0.0373460,\ a_3=0.0269303,\ {\rm and}\ a_4=0.00775118\ {\rm at}\ 0.1\le\Gamma\le 5,\ {\rm and}$

$$r_c(\Gamma) = b_0 \tanh\left(\frac{\eta + b_1}{b_2}\right) + b_3, \tag{45}$$

with $b_0=1.127230,\ b_1=-1.410782,\ b_2=1.849019,\ {\rm and}\ b_3=2.066038$ at $5<\Gamma\le 300.$

The compressibility factor of the entire system, which includes the neutralizing background, is lower than the ionic one, and therefore requires a significantly smaller

cutoff length. However, for $r_c < 1$, the number of reciprocal lattice vectors required for the long-range (reciprocal space) part, $k_c \sim \ln(\varepsilon_0^{-2})/r_c$, increases rapidly, leading to excessive memory usage. This memory limitation is the main reason for the unclear results obtained when attempting to determine the proper cutoff length for the full-system compressibility factor, as well as for the large uncertainty in the region $\Gamma < 1$. Thus, the uncertainty shown in Fig. 11 is calculated as a difference between the approximation of r_c in the last successful run and the previous approximation. Such failure in r_c determination confirms the main conclusion made in Sec. II B that it is the ionic compressibility factor that is found by the virial from LAMMPS calculations rather than a full compressibility factor of the entire system.

In order to explore other possible effects of the cutoff length, the fluid–solid phase transition in the OCP was studied at $\Gamma=10$ –250 with a step of 10. At each Γ , four simulations were performed: (i) $r_c=14$ with random (fluid) initialization, (ii) $r_c=14$ with the bcc lattice initialization, (iii) $r_c=r_c(\Gamma)$ with random initialization, where $r_c(\Gamma)$ is calculated using Eqs. (44) and (45), and (iv) $r_c=r_c(\Gamma)$ with the bcc lattice initialization. In all four cases, the k-space style ewald was employed. For simulations starting from the fluid phase, the number of ions was set to 29^3 , while for those initialized as a bcc lattice, $N=10^3$ was used.

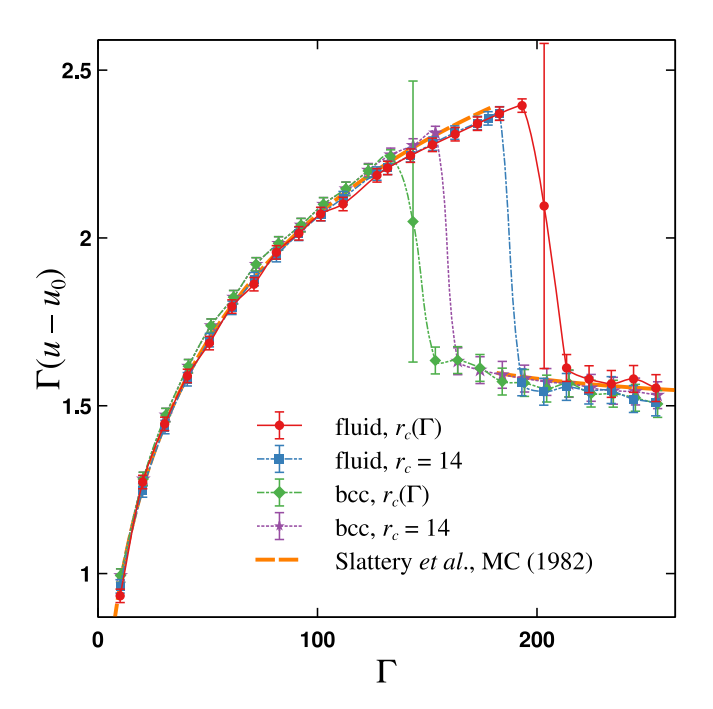


Figure 12. Thermal fraction of the potential energy as a function of the Coulomb coupling parameter for OCP. Circles and diamonds correspond to the simulation with $r_c(\Gamma)$ (44) and (45) and squares and stars, to $r_c=14$. The results from random (fluid, circles and squares) and bcc (solid, diamonds and stars) initialization are shown. Dashed line indicates curve fit of the results from study [43]; lines connecting dots are guides for the eye.

The thermal fraction of the potential energy calculated from the system potential energy as $\Gamma(u-u_0)$ is shown in Fig. 12, where uncertainties are calculated as a difference in the averaged results between simulations performed under the same conditions but using different initial random number generator seeds. All simulation protocols reproduce the known dependence of this quantity, closely following the MC results by Slattery et al. [43]. The choice of different cutoff lengths $(r_c = 14 \text{ or } r_c(\Gamma))$ has a little effect, and both the fluid and bcc initializations converge to almost identical values in a single-phase state. This demonstrates that in the single-phase regime, the system equilibrates effectively, regardless of the initialization type and cutoff treatment. In contrast, differences become apparent near the fluid-solid transition. With the optimized cutoff $r_c(\Gamma)$, simulations initialized in the fluid state exhibit a sharp transition at $\Gamma = 180-200$, while runs with fixed $r_c = 14$ display the transition shifted to lower Γ , though following the same trend. For the bcc initialization, the system with $r_c = 14$ undergoes the transition near $\Gamma \approx 150$, whereas those using the optimized $r_c(\Gamma)$ show the transition delayed to higher Γ . Overall, the metastable region of the OCP proves to be narrower when a fixed cutoff is used, while the optimized $r_c(\Gamma)$ yields significantly broader metastability window. Such behavior can be rationalized in terms of the dependence of the compressibility factor on the cutoff length. Smaller cutoff values reduce the virial contribution, thereby decreasing the effective surface tension. A lower surface tension reduces the Gibbs free energy barrier for nucleation $\Delta G \sim \sigma^3$ and enhances the nucleation rate $J \sim \exp(-\Delta G/T)$ thus making the emergence of phase transition earlier.

V. CONCLUSION

In this study, we employed the model of BOCP to investigate the thermodynamic limit of a system of ions on the compensating background without introducing the PBC. This objective was reached due to discovered universal form of the size dependence of system energy, which proved to be accurate enough to be extrapolated to infinite number of the ions in a wide range of the Coulomb coupling parameter from 0.03 to 1000. This enabled us to avoid the Ewald summation procedure and estimate the energies of a system, which is free from the additional strong interionic correlations imposed by the PBC. A very small width of the metastable region near the BOCP melting point makes it possible to evaluate its position, which amounts to $\Gamma_{\rm m}=174\pm2$. Also, we have introduced three converging quantities in addition to the system energy, namely, the excess interatomic electrostatic energy, the excess ion-background electrostatic energy, and the ionic pressure (compressibility factor), which we determined in the MD simulation. These quantities satisfy the limit conditions that follow from the theory. We show that neither the ionic pressure can be obtained from

the energy of entire system nor the excess pressure of the entire system can be estimated based on the virial determined from MD or MC simulations. We propose an accurate approximation of the ionic compressibility factor and compare it with that calculated for OCP using LAMMPS. We have established that at certain cutoff parameter r_c introduced in LAMMPS, which is characteristic of the ionic interactions, the virial for OCP coincides with that for BOCP. We argue that this is a true virial ensured by a correct choice of r_c , which turns out to be a function of Γ . We present a wide-range approximation of this function for applications. Since r_c defines interionic forces, its correct choice is of crucial importance for the interfacial and dynamic properties of the Coulomb systems including the transport ones. As an example, we simulate the metastable region in the neighborhood of the system melting point with a true r_c and that from the LAMMPS manual. The results are indicative of the fact that for a true r_c , the width of metastable region increases considerably, which points to the increase in the interfacial surface tension. We stress that in every OCP simulation, the obtained virial must be in compliance with the ionic compressibility factor listed in Table II and shown in Fig. 9. Judging from Fig. 10, such compliance must be most important at high Γ .

Apart from revision of our BOCP data for high Γ , an

urgent problem to be addressed in the future is development of a calculation technique that would make it possible to determine the excess interatomic and ion–background energy directly in the simulation of OCP with PBC. Also, calculation of the ionic pressure tensor and phonon spectrum based on these energies are of undoubtful interest.

ACKNOWLEDGMENTS

This work was supported by the Ministry of Science and Higher Education of the Russian Federation (State Assignment No. 075-00270-24-00).

AUTHOR DECLARATIONS

Conflict of Interest

The author has no conflicts to disclose.

DATA AVAILABILITY

The data that support the findings of this study are available within the article.

- [1] M. Baus, Statistical mechanics of simple Coulomb systems, Physics Reports **59**, 1 (1980).
- [2] S. Ichimaru, Strongly coupled plasmas: high-density classical plasmas and degenerate electron liquids, Reviews of Modern Physics 54, 1017 (1982).
- [3] E. V. Kholopov, Convergence problems of Coulomb and multipole sums in crystals, Physics-Uspekhi 47, 965 (2004).
- [4] E. H. Lieb, The Stability of Matter: From Atoms to Stars: Selecta of Elliott H. Lieb, edited by W. Thirring (Springer Berlin Heidelberg, 2005).
- [5] S. Ichimaru, H. Iyetomi, and S. Ogata, Freezing transition and phase diagram of dense carbon-oxygen mixtures in white dwarfs, The Astrophysical Journal 334, L17 (1988).
- [6] G. Chabrier, N. W. Ashcroft, and H. E. DeWitt, White dwarfs as quantum crystals, Nature 360, 48 (1992).
- [7] G. Chabrier, Quantum effects in dense coulumbic matter

 application to the cooling of white dwarfs, The Astrophysical Journal 414, 695 (1993).
- [8] A. Kozhberov, Thermal evolution of old white dwarfs, Journal of Physics: Conference Series 929, 012012 (2017).
- [9] S. Blouin and J. Daligault, Phase separation in ultramassive white dwarfs, The Astrophysical Journal 919, 87 (2021).
- [10] D. A. Baiko, Phase diagrams of binary ionic mixtures and white dwarf cooling, Monthly Notices of the Royal Astronomical Society 517, 3962 (2022).

- [11] Z. Medin and A. Cumming, Crystallization of classical multicomponent plasmas, Physical Review E 81, 036107 (2010).
- [12] M. Iwamatsu, Calculation of the free energy of liquid alkali metal using the non-local pseudopotential— The one-component-plasma and the hard-sphere reference systems, Physica B+C 138, 310 (1986).
- [13] D. J. Wineland, J. C. Bergquist, W. M. Itano, J. J. Bollinger, and C. H. Manney, Atomic-ion Coulomb clusters in an ion trap, Physical Review Letters 59, 2935 (1987).
- [14] D. H. E. Dubin and T. M. O'Neil, Trapped nonneutral plasmas, liquids, and crystals (the thermal equilibrium states), Reviews of Modern Physics 71, 87 (1999).
- [15] O. Arp, D. Block, A. Piel, and A. Melzer, Dust Coulomb balls: Three-dimensional plasma crystals, Physical Review Letters 93, 165004 (2004).
- [16] O. Arp, D. Block, M. Klindworth, and A. Piel, Confinement of Coulomb balls, Physics of Plasmas 12, 122102 (2005).
- [17] S. Käding and A. Melzer, Three-dimensional stereoscopy of Yukawa (Coulomb) balls in dusty plasmas, Physics of Plasmas 13, 090701 (2006).
- [18] H. Totsuji, T. Ogawa, C. Totsuji, and K. Tsuruta, Structure of spherical Yukawa clusters, Journal of Physics A: Mathematical and General 39, 4545 (2006).
- [19] S. W. S. Apolinario, J. A. Aguiar, and F. M. Peeters, Angular melting scenarios in binary dusty-plasma Coulomb balls: Magic versus normal clusters, Physical Review E

- **90**, 063113 (2014).
- [20] D. I. Zhukhovitskii, V. N. Naumkin, A. I. Khusnulgatin, V. I. Molotkov, and A. M. Lipaev, Dust coupling parameter of radio-frequency-discharge complex plasma under microgravity conditions, Physical Review E 96, 043204 (2017).
- [21] D. Huang, M. Baggioli, S. Lu, Z. Ma, and Y. Feng, Revealing the supercritical dynamics of dusty plasmas and their liquidlike to gaslike dynamical crossover, Physical Review Research 5, 013149 (2023).
- [22] M. A. Pokrant, Thermodynamic properties of the nonzero-temperature, quantum-mechanical, onecomponent plasma, Physical Review A 16, 413 (1977).
- [23] D. Ceperley, Ground state of the fermion one-component plasma: A Monte Carlo study in two and three dimensions, Physical Review B 18, 3126 (1978).
- [24] D. A. Baiko, D. G. Yakovlev, H. E. De Witt, and W. L. Slattery, Coulomb crystals in the harmonic lattice approximation, Physical Review E 61, 1912 (2000).
- [25] A. Chugunov, D. Baiko, D. Yakovlev, H. De Witt, and W. Slattery, Pair distribution of ions in Coulomb crystals, Physica A: Statistical Mechanics and its Applications 323, 413 (2003).
- [26] A. Chugunov and D. Baiko, Anharmonic corrections to the electrostatic energy of a Coulomb crystal, Physica A: Statistical Mechanics and its Applications 352, 397 (2005).
- [27] R. T. Farouki and S. Hamaguchi, Thermodynamics of strongly-coupled Yukawa systems near the onecomponent-plasma limit. II. molecular dynamics simulations, The Journal of Chemical Physics 101, 9885 (1994).
- [28] S. Hamaguchi and R. T. Farouki, Thermodynamics of strongly-coupled Yukawa systems near the onecomponent-plasma limit. I. derivation of the excess energy, The Journal of Chemical Physics 101, 9876 (1994).
- [29] S. Hamaguchi, R. T. Farouki, and D. H. E. Dubin, Phase diagram of Yukawa systems near the one-componentplasma limit revisited, The Journal of Chemical Physics 105, 7641 (1996).
- [30] J. M. Caillol and D. Gilles, Numerical simulations of screened Coulomb systems. A comparison between hyperspherical and periodic boundary conditions, Journal of Statistical Physics 100, 905 (2000).
- [31] J. M. Caillol and D. Gilles, Monte Carlo simulations of the Yukawa one-component plasma, Journal of Statistical Physics 100, 933 (2000).
- [32] S. A. Khrapak and A. G. Khrapak, Simple thermodynamics of strongly coupled one-component-plasma in two and three dimensions, Physics of Plasmas 21, 104505 (2014).
- [33] D. A. Young, E. M. Corey, and H. E. DeWitt, Analytic fit to the one-component-plasma structure factor, Physical Review A 44, 6508 (1991).
- [34] N. V. Brilliantov, Accurate first-principle equation of state for the one-component plasma, Contributions to Plasma Physics 38, 489 (1998).
- [35] G. Chabrier and A. Y. Potekhin, Equation of state of fully ionized electron-ion plasmas, Physical Review E 58, 4941 (1998).
- [36] J. M. Caillol, Numerical simulations of Coulomb systems: A comparison between hyperspherical and periodic boundary conditions, The Journal of Chemical Physics 111, 6528 (1999).

- [37] J. M. Caillol, A new (and better) lower bound for the excess internal energy of the one-component plasma, The Journal of Chemical Physics 111, 9695 (1999).
- [38] N. Brilliantov, V. Malinin, and R. Netz, Systematic field-theory for the hard-core one-component plasma, The European Physical Journal D Atomic, Molecular and Optical Physics 18, 339 (2002).
- [39] S. A. Khrapak and A. G. Khrapak, Internal energy of the classical two- and three-dimensional one-componentplasma, Contributions to Plasma Physics 56, 270 (2016).
- [40] S. G. Brush, H. L. Sahlin, and E. Teller, Monte Carlo study of a one-component plasma. I, The Journal of Chemical Physics 45, 2102 (1966).
- [41] J. P. Hansen, Statistical mechanics of dense ionized matter. I. Equilibrium properties of the classical onecomponent plasma, Physical Review A 8, 3096 (1973).
- [42] W. L. Slattery, G. D. Doolen, and H. E. DeWitt, Improved equation of state for the classical one-component plasma, Physical Review A 21, 2087 (1980).
- [43] W. L. Slattery, G. D. Doolen, and H. E. DeWitt, N dependence in the classical one-component plasma monte carlo calculations, Physical Review A 26, 2255 (1982).
- [44] S. Ogata and S. Ichimaru, Critical examination of n dependence in the Monte Carlo calculations for a classical one-component plasma, Physical Review A 36, 5451 (1987).
- [45] J. M. Caillol, Thermodynamic limit of the excess internal energy of the fluid phase of a one-component plasma: A Monte Carlo study, The Journal of Chemical Physics 111, 6538 (1999).
- [46] J.-M. Caillol and D. Gilles, An accurate equation of state for the one-component plasma in the low coupling regime, Journal of Physics A: Mathematical and Theoretical 43, 105501 (2010).
- [47] G. S. Demyanov and P. R. Levashov, One-component plasma of a million particles via angular-averaged Ewald potential: A Monte Carlo study, Physical Review E 106, 015204 (2022).
- [48] R. T. Farouki and S. Hamaguchi, Thermal energy of the crystalline one-component plasma from dynamical simulations, Physical Review E 47, 4330 (1993).
- [49] E. L. Pollock and J. P. Hansen, Statistical mechanics of dense ionized matter. II. Equilibrium properties and melting transition of the crystallized one-component plasma, Physical Review A 8, 3110 (1973).
- [50] J. D. Weeks, Volume change on melting for systems with inverse-power-law interactions, Physical Review B 24, 1530 (1981).
- [51] S. Nordholm, Simple analysis of the thermodynamic properties of the one-component plasma, Chemical Physics Letters 105, 302 (1984).
- [52] J. W. Lee and F. H. Ree, Perturbation theory of a classical one-component plasma, Physical Review A 38, 5714 (1988).
- [53] C. N. Likos and N. W. Ashcroft, Self-consistent theory of freezing of the classical one-component plasma, Physical Review Letters 69, 316 (1992).
- [54] N. Yu, D. Huang, S. Lu, S. Khrapak, and Y. Feng, Universal scaling of transverse sound speed and its isomorphic property in Yukawa fluids, Physical Review E 109, 035202 (2024).
- [55] S. A. Khrapak, Y.-F. Wu, and C.-R. Du, A binary collision approach in one-component plasma: How close to the Frenkel line can we go?, Physics of Plasmas 32,

- 092114 (2025).
- [56] P. P. Ewald, Die Berechnung optischer und elektrostatischer Gitterpotentiale, Annalen der Physik 369, 253 (1921).
- [57] B. Nijboer and F. De Wette, On the calculation of lattice sums, Physica **23**, 309 (1957).
- [58] N. Karasawa and W. A. Goddard, Acceleration of convergence for lattice sums, The Journal of Physical Chemistry 93, 7320 (1989).
- [59] E. Yakub and C. Ronchi, An efficient method for computation of long-ranged Coulomb forces in computer simulation of ionic fluids, The Journal of Chemical Physics 119, 11556 (2003).
- [60] G. S. Demyanov, A. S. Onegin, and P. R. Levashov, N-convergence in one-component plasma: Comparison of Coulomb, Ewald, and angular-averaged Ewald potentials, Contributions to Plasma Physics 64, e202300164 (2024).
- [61] The Stability of Matter: From Atoms to Stars: Selecta of Elliott H. Lieb (Springer Berlin Heidelberg, 2001).
- [62] D. I. Zhukhovitskii and E. E. Perevoshchikov, Structural transition in strongly coupled Coulomb clusters, High Temperature 62, 421 (2024).
- [63] A. S. Onegin, G. S. Demyanov, and P. R. Levashov, Pressure of Coulomb systems with volume-dependent long-range potentials, Journal of Physics A: Mathematical and

- Theoretical 57, 205002 (2024).
- [64] E. S. Shpil'ko and D. I. Zhukhovitskii, Relevance of the Wigner–Seitz cell approximation for the Coulomb clusters, Plasma Physics Reports 49, 1207 (2023).
- [65] L. D. Landau and E. M. Lifshitz, Statistical Physics, Vol. 5 (Elsevier, Oxford, 1980).
- [66] N. Itoh and S. Ichimaru, Harmonic-lattice model for the internal energy of the classical one-component plasma fluid near the crystallization point, Physical Review A 22, 1318 (1980).
- [67] R. Hockney and J. Eastwood, Computer Simulation Using Particles (CRC Press, 2021).
- [68] D. I. Zhukhovitskii, Multiscale approach to the theory of nonisothermal homogeneous nucleation, The Journal of Chemical Physics 160, 194505 (2024).
- [69] A. P. Thompson, H. M. Aktulga, R. Berger, D. S. Bolintineanu, W. M. Brown, P. S. Crozier, P. J. in 't Veld, A. Kohlmeyer, S. G. Moore, T. D. Nguyen, R. Shan, M. J. Stevens, J. Tranchida, C. Trott, and S. J. Plimpton, LAMMPS a flexible simulation tool for particle-based materials modeling at the atomic, meso, and continuum scales, Computer Physics Communications 271, 108171 (2022).
- [70] M. Bolten, F. Fahrenberger, R. Halver, F. Heber, M. Hofmann, I. Kabadshow, O. Lenz, M. Pippig, and G. Sutmann, ScaFaCoS, C subroutine library, http://scafacos.github.com/.